Research Article | Vol. 30, No. 21 / 10 Oct 2022 / Optics Express 38596
Optics EXPRESS

# Photonic-assisted 2-D terahertz beam steering enabled by a LWA array monolithically integrated with a BFN

THOMAS HADDAD,[1,*] CARLOS BIURRUN-QUEL,[2] PENG LU,[1] JONAS TEBART,[1] BENEDIKT SIEVERT,[3] SUMER MAKHLOUF,[1] MARCEL GRZESLO,[1] JORGE TENIENTE,[2] CARLOS DEL-RÍO,[2] AND ANDREAS STÖHR[1]

[1]*Center for Semiconductor Technology and Optoelectronics (ZHO), University of Duisburg-Essen, Lotharstr. 55, LT building, 47057 Duisburg, Germany*
[2]*Antenna Group | Institute of Smart Cities, Electric, Electronic and Communication Engineering Department. Campus de Arrosadía, E-31006 Pamplona-Navarra, Spain*
[3]*Department of ATE, Faculty of Engineering, University of Duisburg-Essen, Bismarckstr. 81, BA Building, 47057 Duisburg, Germany*
[*]*thomas.haddad@uni-due.de*

**Abstract:** A novel photonic-assisted 2-D Terahertz beam steering chip using only two tuning elements is presented. The chip is based on an array of three leaky wave antennas (LWAs) with a monolithically integrated beamforming network (BFN) on a 50 µm-thick indium phosphide substrate. The THz beam angle in elevation (*E*-plane) is controlled via optical frequency tuning using a tunable dual-wavelength laser. An optical delay line is used for azimuth (*H*-plane) beam control. The simulated beam scanning range is 92° in elevation for a frequency sweep from 0.23 THz to 0.33 THz and 69.18° in azimuth for a time delay of 3.6 ps. For the frequency range from 0.26 THz to 0.32 THz, it is confirmed experimentally that the THz beam scans from −12° to +33°, which is in good agreement with the numerical simulations. The beam direction in azimuth scans with a total angle of 39° when applying a delay difference of 1.68 ps. A good agreement is found between theoretically predicted and experimentally determined THz beam angles with a maximum angle deviation below 5°. The experimental scanning angles are limited due to the mechanical constraints of the on-wafer probes, the on-chip integrated transition and the bandwidth of the THz receiver LNA. The mechanical limitation will be overcome when using a packaged chip.



## 1. Introduction

The lower part of the Terahertz (THz) spectrum (0.1–1 THz) offers a lot of attractive features for several applications, including medical screenings (lower energy than X-Rays) [1,2], imaging (higher resolution than microwaves) [2,3], radar [4], spectroscopy [5,6], short-range communications [7,8], and future mobile THz communications such as 6G [9–11].

A generic challenge for THz applications is to overcome the free-space path loss (FSPL), which is proportional to the square of the carrier frequency [12] and thus is more dominant in the THz regime than for microwave frequencies. To mitigate FSPL, high THz transmit power and high gain THz antennas are necessary. In addition, to support mobile users, chip-to-chip self-alignment [13], and machine-to-machine (M2M) communications, the THz antennas must also provide beam steering capabilities.

Among different THz source technologies, III/V semiconductor-based THz photodiodes (PDs) have attracted great interest since they offer ultra-wideband operation, which is a crucial requirement for many THz applications, including spectroscopy or high data rate mobile

#468200 https://doi.org/10.1364/OE.468200
Journal © 2022 Received 20 Jun 2022; revised 24 Aug 2022; accepted 26 Aug 2022; published 3 Oct 2022

Optics EXPRESS

communications [14]. However, the output power level from a single THz PD is still limited. Today, the highest reported continuous-wave output power of a single uni-traveling carrier photodiode (UTC-PD) is 750 $\mu$W at 300 GHz [15]. Combining the outputs of several UTC-PDs is one solution to overcome the power bottleneck. In [16], a power combiner for the WR10 frequency band (75–100 GHz) and in [17], a THz power combiner for the WR3.4 frequency band (220–320 GHz) were reported. However, these power combiners are bulky compared to planar integrated THz PD arrays. Therefore, they may not suit applications where compactness and lightweight THz transmitters are mandatory. The preferred technological solution concerning the scalability would thus be a planar or even monolithic integration of an array of THz PDs with THz antennas. This solution would not only increase the total THz transmit power by free-space power combining but also enable the THz beam steering using phase shifters (PSs) or true-time delays (TTDs) in the optical domain [18].

For 1-D THz beam steering, there are many traditional approaches with a solid background in lower frequencies [19,20], and their implementation in the THz regime is practical [21]. The first photonic-assisted linear and planar antenna arrays were recently reported, e.g., a $1 \times 4$-photomixer array with four optical delay lines (ODLs) at 600 GHz [22]. Also, optical phase shifters [23,24] for optical beam control circuits have been introduced. Nevertheless, these concepts are of considerable size, and the complex optical phase shifter or true-time delay feeders impede monolithic integration and limit the scalability of these solutions. In this context, leaky-wave antennas (LWAs) with integrated THz PDs have a distinct advantage, namely a much simpler feeding network than conventional phased arrays. In [25], we reported a periodic photonic-assisted LWA for 1-D THz beam steering based on a microstrip structure on a 50 µm-thick InP wafer. Here, we demonstrated photonic-assisted 1-D THz beam steering with a scanning range of 88° within the WR3.4 band.

Actual control of 2-D THz beam steering systems still accounts for fewer examples. For instance, in [26], at 344 GHz a $2 \times 2$ phased array consisting of standing wave oscillators based on CMOS technology could achieve a scanning angle of 128° and 53° in two directions. In [27], a combination of frequency sweeping and mechanical tilting of a metallic plate to enable the 2-D beam steering is reported.

This paper reports on photonic-assisted 2-D THz beam steering using an integrated on-chip LWA array. In general, for 2-D THz beam steering using phased arrays, $n \times n$ tuning elements are necessary. However, only $n+1$ tuning elements, i.e., $n$ PS or TTD and one tunable dual $\lambda$ laser for beam control, are needed for an approach of $n$ LWAs with integrated $n$ PDs. To further reduce the number of tuning elements, we present a novel 2-D beam steering concept based upon integrating multiple THz PDs to an array of LWAs via a beamforming network (BFN). In our approach, the BFN is based on coherently radiating periodic structures (CORPS-BFN), previously introduced for microwave frequencies [28]. A CORPS-BFN generates a linearly progressive phased distribution at its outputs. Accordingly, depending on the count of layers used for the CORPS-BFN, the inputs can be reduced to two, and only one PS/TTD tuning element is required for one input. Here, we developed a THz CORPS-BFN with two inputs and three outputs ($2 \times 3$ CORPS-BFN). Each output is connected to an individual LWA. This way, we successfully reduce the number of tuning elements for 2-D THz beam steering to only two, one PS for azimuth control and, one frequency tunable dual $\lambda$ laser for elevation control. To the best of our knowledge, this is the first report on a photonic-assisted 2-D THz beam steering chip and the first concept enabling 2-D beam steering with only two control elements. In addition, the technological implementation of III/V semiconductors enables planar or even monolithic integration of the antenna array with active THz sources and detectors. Therefore, the approach paves the way for future THz photonic/electronic transceiver chips featuring 2-D beam steering.

This manuscript is organized as follows: at first, the concept for 2-D beam steering using a $2 \times 3$ CORPS-BFN and a LWA array is introduced. Then, the design of the antenna and the $2 \times 3$

Optics EXPRESS

CORPS-BFN are presented. Next, the chip fabrication and experimental characterization of the S-parameters for the fabricated structure are discussed. Finally, simulated and measured 2-D THz beam steering capabilities are reported.

## 2. Photonic-assisted 2-D THz beam steering concept

Conventional concepts for 2-D beam steering using an $n\times n$ phased array require one phase or time tuning element for each antenna. Therefore, the number of tuning elements increases quadratically with the number of antenna elements [29,30]. For example, the system in [22] requires four ODLs to manage the $1\times 4$ phased array.

In this work, we propose a photonic-assisted 2-D beam steering concept requiring only two control elements, one ODL and one tunable dual $\lambda$ laser. This is achieved by integrating an array of THz LWAs with a THz CORPS-BFN, as illustrated in Fig. 1.

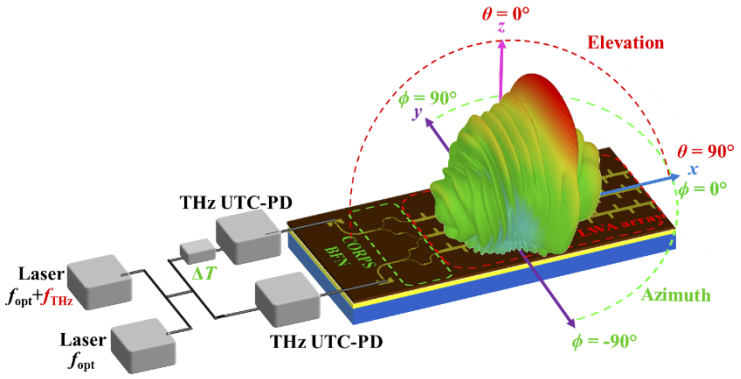


**Fig. 1.** The concept of photonic-assisted 2-D beam steering using an array of LWAs for steering in elevation angle $\theta$ based on the applied frequency $f_{\mathrm{THz}}$ (red) and a CORPS-BFN for steering azimuth angle $\phi$ based on the applied time delay $\Delta T$ (green).

An optical heterodyning set-up generates a frequency-tunable THz signal, which is then fed to the LWAs through a broadband CORPS-BFN, causing the emerged THz beam to sweep in elevation $\theta$ direction. In addition, thanks to the CORPS-BFN, a linearly progressive phase shift is introduced between the adjacent LWAs, which steers the radiated THz beam in azimuth $\phi$ direction. To control the phase shift $\Delta\varphi$, an ODL is used. As will be explained in the next section, a phase change of $\Delta\varphi$ between the two input ports of the THz CORPS-BFN will be distributed to a phase difference of $\Delta\varphi/2$ between two adjacent antennas. The correspondence between time and phase is given by [30]:

$$\Delta T = \frac{\lambda\cdot\Delta\varphi}{2\cdot\pi\cdot c_0} = \frac{\Delta\varphi}{2\cdot\pi\cdot f}, \tag{1}$$

where $c_0$ is the speed of light in vacuum, $\lambda$ and $f$ represent wavelength and frequency of the THz beam, respectively. As explained by the array theory for 2-D planar arrays [18], the direction of the maximum radiation of the array factor, given by $\phi$ and $\theta$ angles is defined by the following equations:

$$\phi = \tan^{-1}\left(\frac{\beta_y\cdot d_x}{\beta_x\cdot d_y}\right), \text{ and} \tag{2-a}$$

$$\theta = \sin^{-1}\left(\sqrt{\left(\frac{\beta_x}{k\cdot d_x}\right)^2+\left(\frac{\beta_y}{k\cdot d_y}\right)^2}\right) \tag{2-b}$$

Optics EXPRESS

where $k$ is the wavenumber, $k = 2\pi/\lambda$. In the proposed antenna concept, the array element spacing along the $x$-axis '$d_x$' is the length of a LWA unit cell and the array element spacing along the $y$-axis $d_y$ corresponds to the spacing between the LWAs. The progressive phase along the LWA $\beta_x$ is given by $\beta_x = \beta_{\text{unit cell}} \cdot d_x$, where $\beta_{\text{unit cell}}$ is the phase constant of a LWA unit cell. The progressive phase shift between the adjacent LWAs $\beta_y$ is given by $\beta_y = \Delta\varphi/2$. For Eqs. (2-a) and (2-b), it can be seen that, as in all 2-D steering concepts, the azimuth and elevation angles $\phi$ and $\theta$, respectively, are not completely independent. This relation is shown in Eqs. (3-a) and (3-b):

$$\phi(f, \Delta T) = \tan^{-1}\left(\frac{\Delta\varphi}{2 \cdot \beta_{unit.cell} \cdot d_y}\right) = \tan^{-1}\left(\frac{\pi \cdot f \cdot \Delta T}{\beta_{unit.cell} \cdot d_y}\right) \tag{3-a}$$

$$\begin{aligned}\theta(f, \Delta T) &= \sin^{-1}\left(\sqrt{\left(\frac{\beta_{unit.cell}}{k}\right)^2 + \left(\frac{\Delta\varphi}{2 \cdot k \cdot d_y}\right)^2}\right) \\ &= \sin^{-1}\left(\sqrt{\left(\frac{\beta_{unit.cell}}{k}\right)^2 + \left(\frac{\pi \cdot f \cdot \Delta T}{k \cdot d_y}\right)^2}\right)\end{aligned} \tag{3-b}$$

## 3. Chip design

### 3.1. THz antenna

Our previous work [25] developed an InP-based periodic THz 1-D LWA for monolithic integration with THz photodiodes (PDs). Using a substrate-transfer technology, the LWAs were fabricated on a 50 µm-thin InP substrate to reduce the number of surface-wave modes to the $TM_0$ mode for a higher radiation efficiency [31]. However, the first LWAs were suffering from the open-stop band (OSB) issue (see grey curves in Fig. 2(a)), where the counter-directional coupling of space harmonics leads to a drastically reduced gain at the broadside [25]. In this work, we redesigned the unit-cell by introducing a matching stub to suppress the OSB effect [32], as presented in the inset in Fig. 2(a). The proposed antenna design is simulated and analyzed using the full-wave commercial electromagnetics (EM) solver Dassault Systems CST Studio 2021. The scattering parameters of the optimized antenna (black curves) are plotted in Fig. 2(a). As can be seen, the return loss is below 17 dB in most of the WR3.4 frequency band and about 13.8 dB around 0.273 THz, which is the broadside frequency where the $\beta_{\text{unit cell}}$ is close to zero. The dimensions of the designed unit cell are shown in Fig. 2(b).

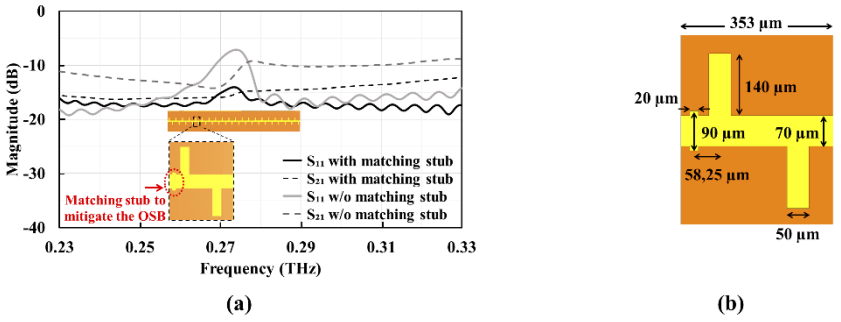


**Fig. 2.** (a) Simulated scattering parameters of designed LWA in comparison with the previous work in [25] (grey curves). The inset shows a schematic top view of the microstrip periodic LWA and a close-up of a single unit-cell. (b) Geometry and dimensions of the single unit cell.

Optics EXPRESS

The dispersion diagram of a single unit cell is provided in Fig. 3(a). The phase constant is smaller than the free-space propagation constant (light line), allowing the radiation of fast waves by the LWA. The attenuation constant $\alpha$ of a single unit cell increases around the broadside resulting in mitigation of the OSB effect, but this enhancement does not lead to a higher realized gain in the broadside region than in the rest domain, as can be seen in Fig. 3(b). This can be explained with respect to Fig. 2(a), where an impedance mismatching in the broadside region counteracts the enhancement. Overall, the designed antenna covers an entire quadrant with a scanning range of 92° degrees. As can be seen from Fig. 3(b), the radiation angle is $\theta = -50°$ at 0.23 THz and $\theta = 42°$ at 0.33 THz. For more clarity, the polar diagram of the simulated far-field radiation patterns of the LWA is added in Fig. 3(c).

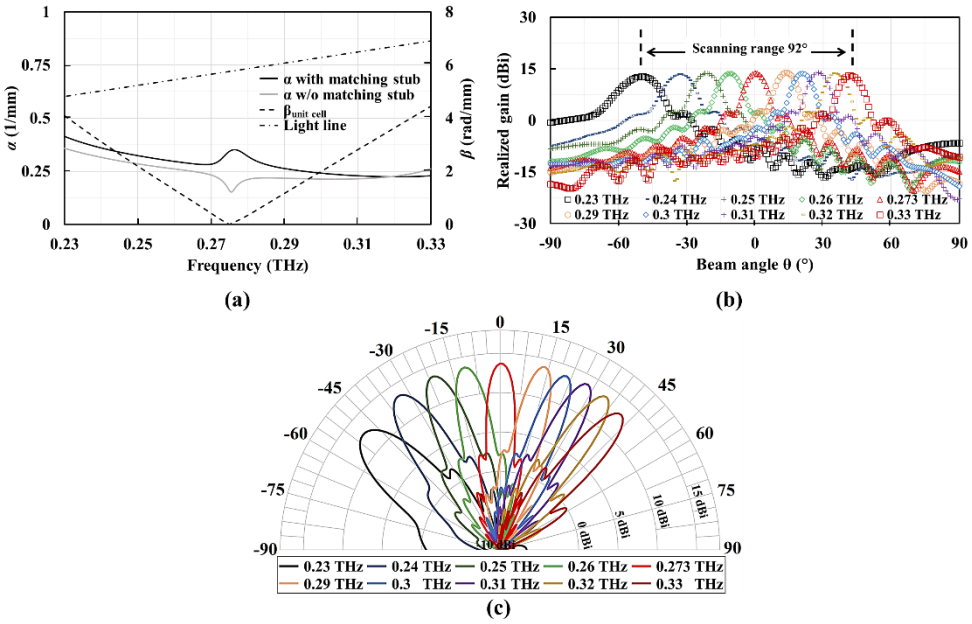


**Fig. 3.** (a) Simulated dispersion diagram of a single unit cell. (b) Simulated realized gain for the designed microstrip LWA at different angles in the $H$-plane. (c) Polar diagram of the simulated far-field radiation patterns of the LWA in $H$-plane.

### 3.2. THz CORPS beamforming network

As introduced in section 2, a CORPS-BFN generates a linear progressive phase distribution at the output elements of the network. This network is based on cascaded Wilkinson power combiners/dividers (WPCDs) in a multi-layer formation [33]. The WPCDs are called recombination nodes ($R$-node) when acting as a combiner or split nodes ($S$-node) in the case of a divider. The key element of a WPCD is a resistor, which guarantees the isolation between the adjacent inputs ($R$-nodes operation) or outputs ($S$-nodes operation) and matching the impedance of the output ports of the network.

This section discusses the concept of a single layer CORPS-BFN consisting of two $S$-nodes and a single $R$-node to form a network of two inputs and three outputs ($2 \times 3$ CORPS-BFN), as depicted in Fig. 4(a). The principle of operation is explained by considering two input signals $s_1(t)$ and $s_2(t)$ having the same amplitude and a phase difference of $\Delta\varphi$. After the transmission

Optics EXPRESS

through the $S$-nodes (S1 and S2), they are divided into $s_{1a}(t)$, $s_{1b}(t)$, $s_{2a}(t)$, and $s_{2b}(t)$, as follows:

$$\begin{aligned} S_{1a}(t) = S_{1b}(t) &= \frac{A}{\sqrt{2}} \cdot \cos(\omega t) \ldots [V/m], \\ S_{2a}(t) = S_{2b}(t) &= \frac{A}{\sqrt{2}} \cdot \cos(\omega t - \Delta\varphi) \ldots [V/m]. \end{aligned} \tag{4}$$

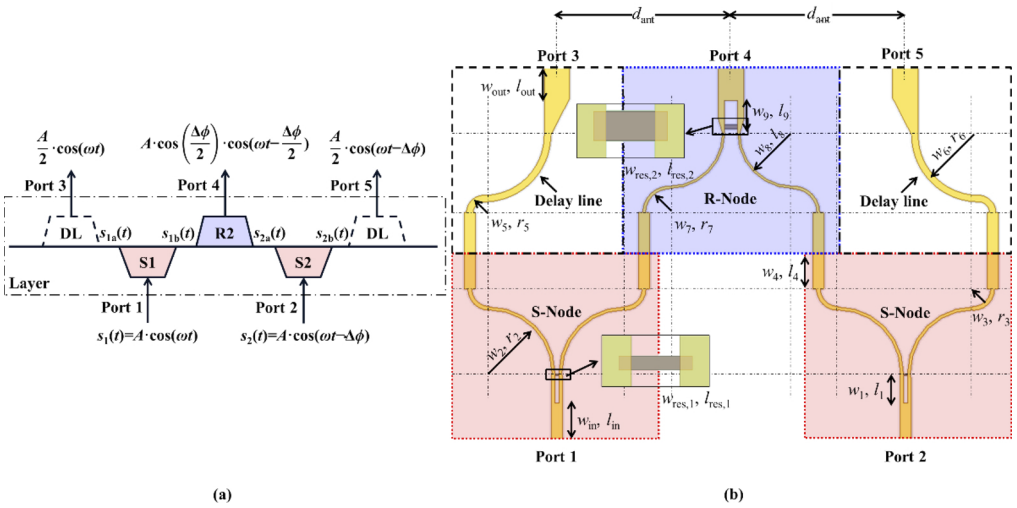


**Fig. 4.** (a) Generation of linearly progressive phase distribution in a 2 × 3 CORPS-BFN.(b) Outline of the fabricated 2 × 3 CORPS-BFN. S-nodes are highlighted in red, and R-nodein blue.

Identical phase response is expected since every $S$-node is built upon the same WPCD. In the next step, each signal will reach the connected $R$-nodes. In the 2 × 3 CORPS-BFN network, the two outer $R$-nodes are replaced by delay lines, so the signals $s_{1a}(t)$ and $s_{2b}(t)$ will be delivered directly to the ports 3 and 5. Only port 4 at the output of the recombination node R2 receives contributions from both input signals. The following equation describes the recombination taking place at R2:

$$\begin{aligned} S_{out,R2}(t) &= \frac{1}{\sqrt{2}}(S_{1b}(t) + S_{2a}(t)) = \frac{A}{2} \cdot [\cos(\omega t) + \cos(\omega t - \Delta\varphi)] \ldots [V/m], \\ S_{out,R2}(t) &= A \cdot \cos\left(\frac{\Delta\varphi}{2}\right) \cdot \cos\left(\omega t - \frac{\Delta\varphi}{2}\right) \ldots [V/m]. \end{aligned} \tag{5}$$

The $R$-node is considered lossless, so the nominal transmission parameter $(1/\sqrt{2})$ is applied. As can be seen from Fig. 4(a) and the equations above, the CORPS-BFN generates a linear progressive phase distribution with a relative phase of 0, $\Delta\varphi/2$, and $\Delta\varphi$ at its three outputs. As discussed in [34], increasing the number of output ports, i.e., increasing the number of connected LWAs, can be done by increasing the number of the CORPS-BFN layers. However, this comes at the expense of higher losses and reduced scan, imposing a trade-off between array size and overall efficiency. Furthermore, as can be seen from Eq. (5), the output amplitude is proportional to $\cos(\Delta\varphi/2)$. Thus the efficiency of the 2-D antenna array depends on the steering angle. Nevertheless, as demonstrated further below, this degradation is comparably minor.

The layout of a single layer 2 × 3 THz CORPS-BFN is shown in Fig. 4(b). The outputs' separation ($d_{ant}$) is fixed at 480 µm, defined by the recommended antenna spacing at the WR3.4 frequency domain. The main parameters of the 2 × 3 THz CORPS-BFN layout are listed in Table 1.

Optics EXPRESS

**Table 1. Parameters of 2 × 3 CORPS-BFN**

| Parameter | Value (μm) | Parameter | Value (μm) | Parameter | Value (μm) | Parameter | Value (μm) |
|---|---|---|---|---|---|---|---|
| $w_1$ | 9 | $l_1$ | 68 | $w_8$ | 6 | $r_8$ | 146 |
| $w_2$ | 8 | $r_2$ | 172 | $w_9$ | 17 | $l_9$ | 53 |
| $w_3$ | 11 | $r_3$ | 54 | $w_{\text{in}}$ | 30 | $l_{in}$ | 100 |
| $w_4$ | 30 | $l_4$ | 42 | $w_{out}$ | 70 | $l_{out}$ | 100 |
| $w_5$ | 18 | $r_5$ | 39 | $w_{res1}$ | 3.4 | $l_{res1}$ | 12 |
| $w_6$ | 18 | $r_6$ | 175 | $w_{res2}$ | 10 | $l_{res2}$ | 36 |
| $w_7$ | 8 | $r_7$ | 70 | | | | |

For impedance matching, the output ports of the CORPS-BFN are tapered to match the LWA's input impedance of 40 Ω, while the input ports have an impedance of 50 Ω. The resistors included in the WPCDs (see insets in Fig. 4(b)) were designed to achieve an input impedance of 100 Ω and were made up of Titanium (Ti) using thin-film technology. Although Titanium is a conductive material, it is oxidized to resistive $TiO_2$ under atmospheric conditions [35], increasing the film's resistivity. The geometries of the resistors were determined from:

$$R = \frac{\rho \cdot L}{w \cdot t} = R_s \cdot \frac{L}{w}, \tag{6}$$

where $\rho$ is the resistivity of the material constituting the resistor and $R_s$, $t$, $L$, and $w$ are the sheet resistance, thickness, length, and width of the film, respectively.

The *four-point probe method* [36] was used to measure the DC conductivity of various samples with different thicknesses. For example, the average DC conductivity was 295 ± 25 kS/m for 200-nm-thick samples of oxidized Ti, which is expected to be decreased in mmWave and THz ranges [37].

Figure 5 provides the main scattering parameters of the designed 2 × 3 THz CORPS-BFN. The reflection coefficients of each port ($S_{11} = S_{22}$ and $S_{33} = S_{55}$ due to symmetry) and the transmission from an input to an output port ($S_{31} = S_{52}$ and $S_{41} = S_{42}$) are depicted in Fig. 5(a). A deviation in the thin-films conductivity was simulated and observed to cause a frequency shift in the response. Nevertheless, the reflection coefficients and isolations remained underneath the 15 d B level in the worst case. Therefore, the transmission towards the output ports remains unaffected. Figure 5(b) provides more details about the transmission coefficient between the isolated ports in the network ($S_{51} = S_{32}$ and $S_{43} = S_{45}$). Since the network is passive, the scattering matrix is reciprocal.

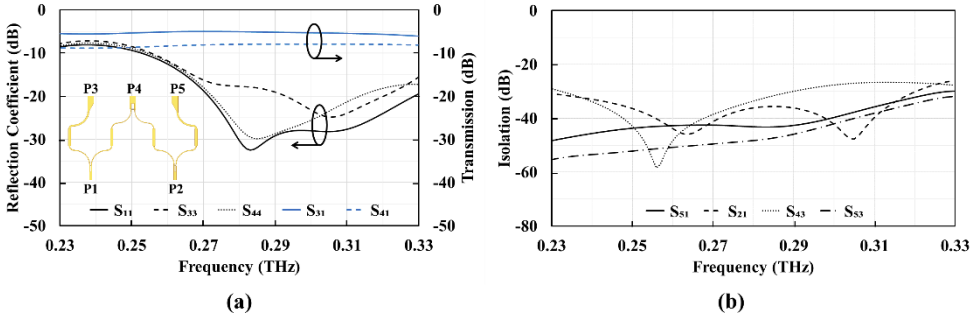


**Fig. 5.** Simulated S-Parameters of the THz 2 × 3 CORPS-BFN. (a) Reflection coefficient (black) and transmission (blue) to ports, (b) Isolation between ports.

A phase difference between $S_{31}$ and $S_{41}$ was observed due to the dissimilarity of the tapered shape of these outputs. This mismatch was lower than 3° within the band. However, when

Optics EXPRESS

assessing a variation in the conductivity of the thin films, these differences increased to 6° at the band's upper end (0.33 THz). Such phase difference would have a detrimental impact on the performance of the BFN if it were higher since the contribution of each antenna would not combine in phase.

Generally, the azimuth beam steering capabilities of $2 \times 3$ CORPS-BFN integrated with an array of three frequency-independent antennas radiating towards the broadside, e.g. bow-tie or patch antennas, can be described by the following equation [30]:

$$\phi = \sin^{-1}\left(\frac{\lambda \cdot \Delta\varphi/2}{2 \cdot \pi \cdot d_{ant}}\right) = \sin^{-1}\left(\frac{c \cdot \Delta\varphi/2}{2 \cdot \pi \cdot f \cdot d_{ant}}\right), \tag{7}$$

The steering angles $\phi$ for different values of $\Delta\varphi$ and $f$ are plotted in Fig. 6(a). The azimuth scanning range increases with $\Delta\varphi$ and reaches the maximum value with $\Delta\varphi = |\pi|$. In addition, the angle $\phi$ is inversely proportional to the frequency. Thus, the maximum scanning range is reduced from 84.74° to 56.02° when increasing the frequency from 0.23 to 0.33 THz.

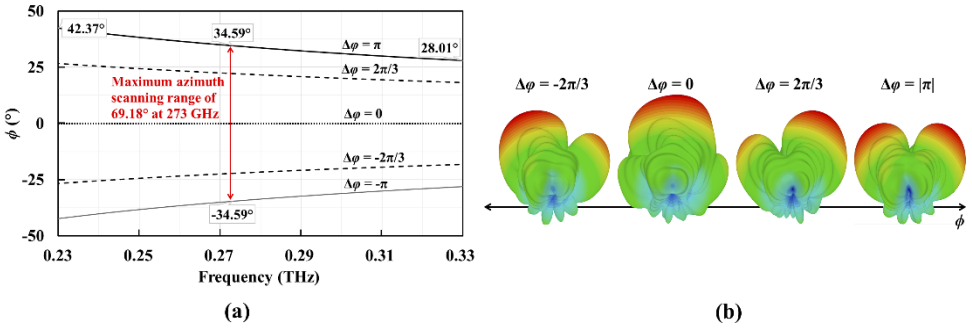


**Fig. 6.** **(a)** Beam angle in azimuth direction at different $\Delta\varphi$ between the inputs of the CORPS-BFN. The maximum beam angle for a SLL of 0 dB corresponds to $\Delta\varphi = \pi$. (b) Radiation pattern in $E$-plane at the elevation broadside frequency $f = 0.273$ THz for different $\Delta\varphi$.

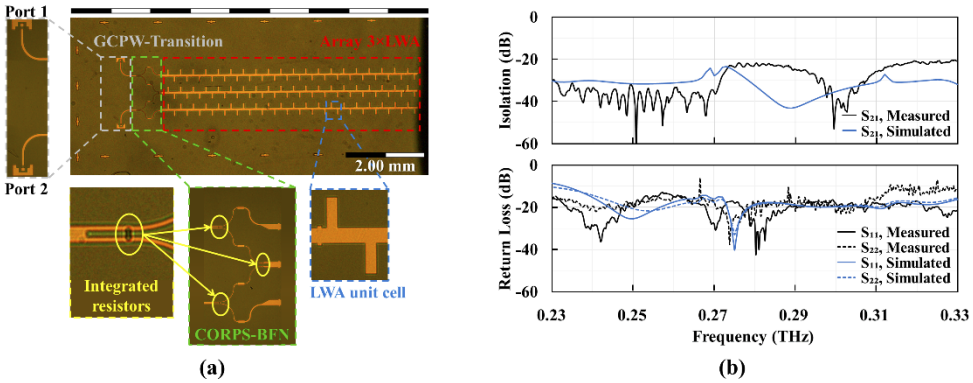


**Fig. 7.** (a) Fabricated structure of an array of three LWA integrated with CORPS-BFN and GCPW transition with a zoom-in of the transition, CORPS-BFN, integrated resistors, and unit cell. (b) The measured scattering parameters for a de-embedded structure of CORPS-BFN and array of three LWAs (black) in comparison with the scattering parameters of a simulated de-embedded structure (blue)

Optics EXPRESS

It is noteworthy that, when integrating the CORPS-BFN with an array of LWA, (7) cannot be applied, as the propagation constant of the LWA ($\beta_{\text{unit cell}}$) will modify the direction of the maximum radiation. This was described in Eqs. (3-a) and (3-b). Due to this dual dependence ($\Delta\varphi$, $\beta_{\text{unit cell}}$), the beam steering capabilities of the LWA array can only be described by (7) at the LWA broadside frequency 0.273 THz, where $\beta_{\text{unit cell}} = 0$. Figure 6(b) sketches this scenario for different phase delays between the input ports. Further information on the beam steering capabilities of the integrated CORPS-BFN with LWA array will be discussed in section 5. The side-lobe level (SLL) increases when $|\Delta\varphi| > 0$. In other words, for a side-lobe suppression of 0 dB, the maximum scanning range of 69.18° corresponds to $\Delta\varphi = |\pi|$ (see Fig. 6(a)), which leads, according to Eq. (5), to disabling the middle output of the CORPS-BFN ($s_{\text{out,R2}}(t) = 0$). Nevertheless, the maximum scanning angle will be reduced for a higher side-lobe suppression, taking into account the same radiative elements. For instance, the simulated scanning range is 34° for a suppression level of 10 dB. It is worth noting that the equivalent $\Delta T$ of each $\Delta\varphi$ can be calculated from Eq. (1), i.e., $\Delta T = 1.8$ ps for $\Delta\varphi = \pi$.

## 4. Chip fabrication

The manufactured chip is shown in Fig. 7(a). Both, the LWA array with a pitch of $d = 480$ µm and the CORPS-BFN are built on a 50 µm-thin InP-substrate. Grounded coplanar waveguide GCPW to microstrip line MSL transitions are used to probe the chip, as seen from the close-up photographs in Fig. 7(a). Also, the integrated planar resistors in the WPCD and the LWA unit can be seen from the close-up pictures. The fabrication process was carried out by standard photolithography, electron beam metal deposition, and lift-off. At first, 220-nm-thick thin-film resistors were fabricated using Ti metal deposition, which is 20 nm thicker than the designed resistors. Next, the coplanar waveguide and microstrip structures of 1.2 µm-thick copper were deposited. Finally, a 75 nm thick gold layer is developed to prevent oxidation. After fabrication, the surface roughness of the deposited metal contacts was measured using a DektakXT stylus profiler revealing an average roughness of 10.7 nm.

The scattering parameters were measured using a Rohde & Schwarz ZVA40 Vector Network Analyzer (VNA), ZC330 Tx/Rx waveguide extender, and a ZRX330 receiver (Rx) module. In addition, an on-chip Thru-Reflect-Line TRL calibration kit [38] was used to de-embed the transitions as well as the effect of the probes employed in the measurement.

The scattering parameters of the CORPS-BFN and LWAs array structure are provided in Fig. 7(b). Here, the transitions were de-embedded from both the measurement and simulation results by applying the known TRL algorithm. As can be seen, the measured isolation and return loss are in good agreement with the simulated performances. Furthermore, the benchmarks, i.e., isolation better than 20 dB and a reflection coefficient below −15 dB, were achieved. The observed discrepancy between the measured and simulated isolation around 0.28 THz is traced back to the uncertainty in the actual impedance of the integrated resistors.

## 5. 2-D THz beam steering

The 2-D beam steering capabilities were simulated using CST by changing the frequency of the inputs (discrete ports) and applying different time shifts on each port. The normalized beam profiles at designated pairs ($f$, $\Delta T$) are plotted in Fig. 8 and Fig. 9, where $f$ is the applied frequency, and $\Delta T$ corresponds to the time shift/delay between ports 1 and 2 (see Fig. 7(a)).

Related to Eqs. (3-a) and (3-b), the beam angle in each direction is affected by both progressive phase shifts $\beta_{\text{unit cell}}$ and $\beta_y$. For instance, the beam angle in elevation $\theta$ for a given frequency can be shifted by ~2° when applying $\Delta T$ of 0.56 ps. On the other hand, the influence on the beam angle in azimuth $\phi$ for a given $\Delta T$ is neglectable when changing the frequency.

Optics EXPRESS

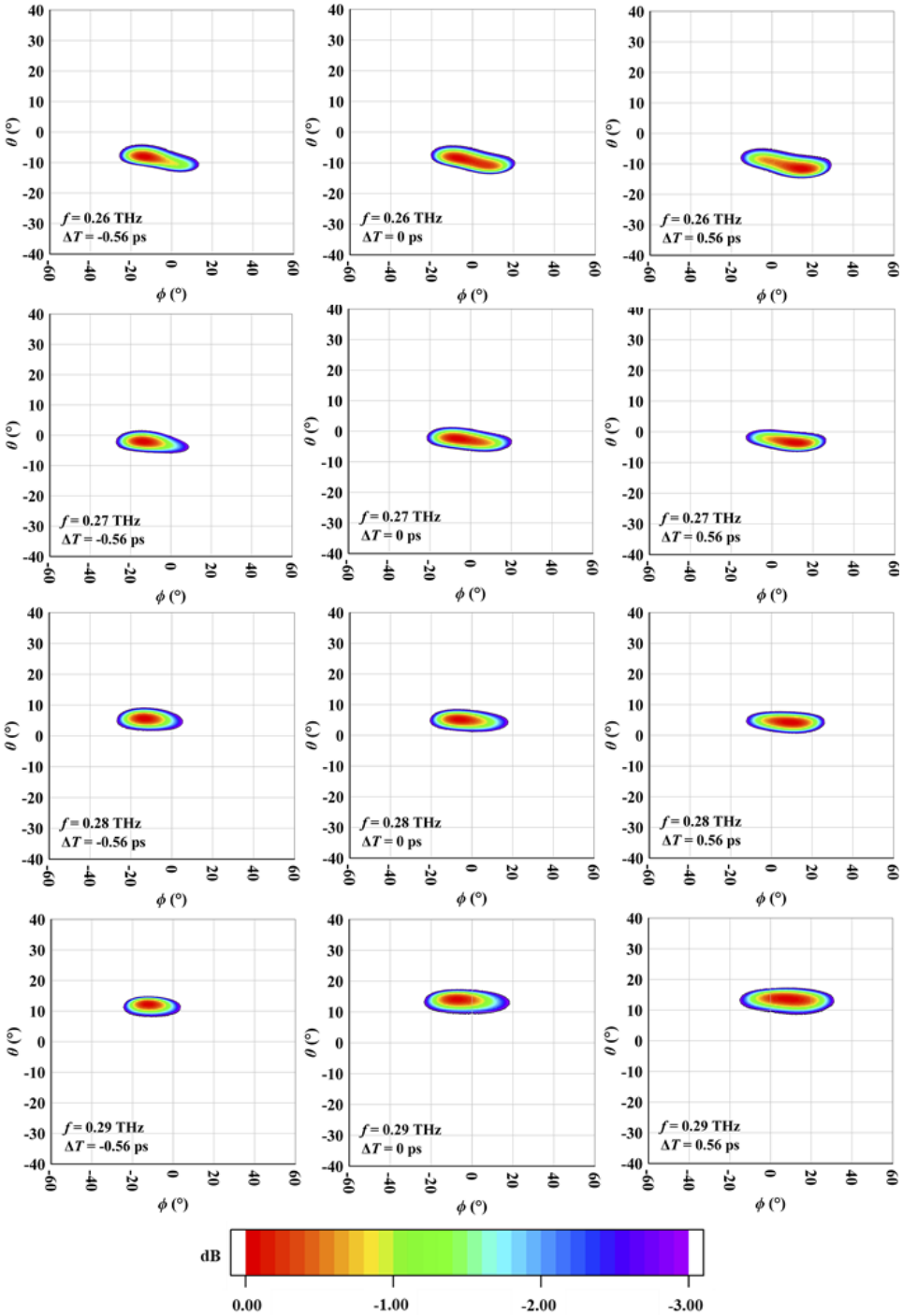


**Fig. 8.** Simulated 3-dB beam profiles between (0.26 and 0.29 THz) anddelay times (0 and ±0.56 ps).

Optics EXPRESS

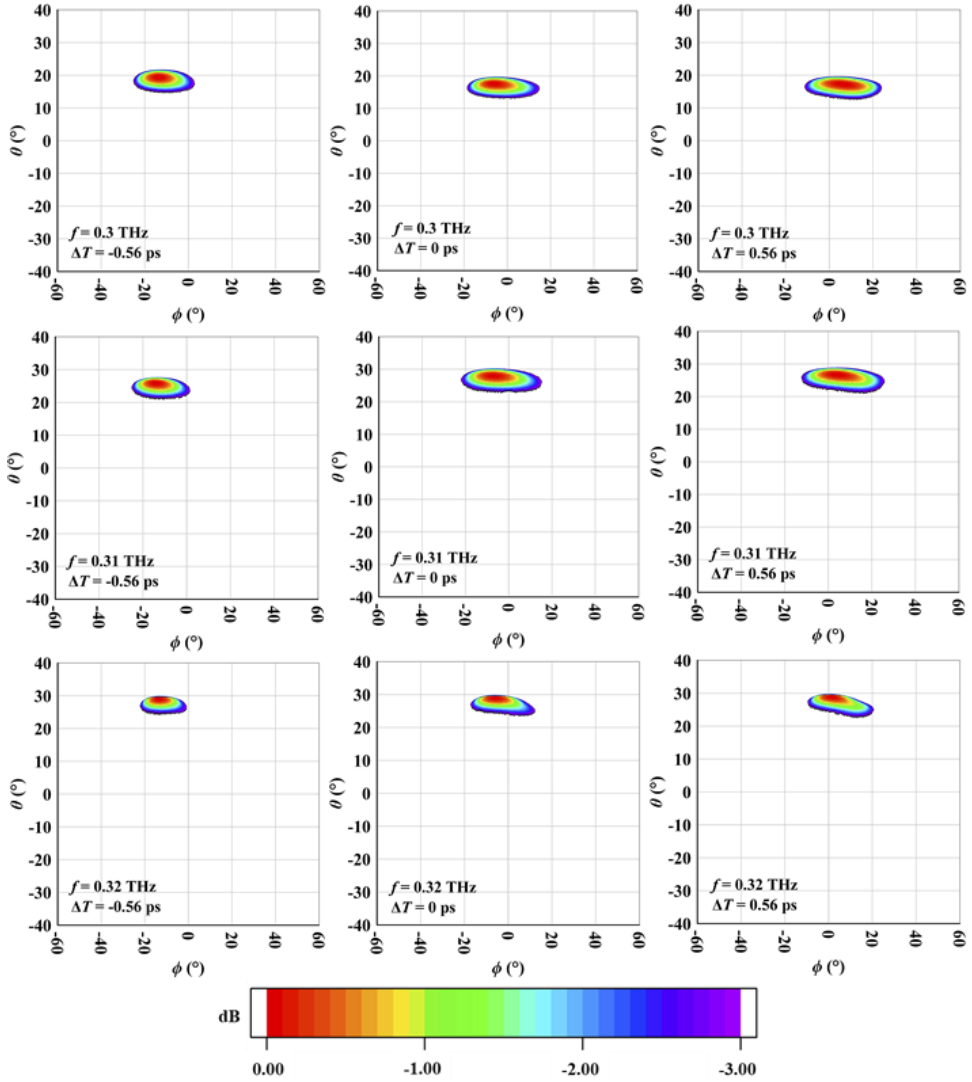


**Fig. 9.** Simulated 3-dB beam profiles between (0.3 and 0.32 THz) anddelay times (0 and ±0.56 ps).

Moreover, it is observed that the beam angle with $\Delta T = 0$ ps is shifted in the $\phi$ direction towards the direction of the first stub of the LWA. To compensate for this effect, an effective calibration technique will be introduced later in this section.

The system set-up in Fig. 10 is used to characterize the 2-D beam steering capabilities of the fabricated chip experimentally. The *THz signal generation* is based on an optical heterodyning architecture exploiting two free-running integrable tunable laser assemblies (ITLA). This way, the frequency difference $\Delta f$ between the two optical carriers defines the desired THz signal. After combining and amplifying the optical signals, they are split into two paths. Each contains a motorized variable optical delay line. It must be mentioned that only ODL1 is used to adjust the time delay when validating 2-D beam steering capabilities. ODL2 is only used to compensate for the fiber length difference and avoid the phase shift fluctuation [39]. Then, the THz signal is converted from optical to electrical domain using a UTC-PD. In addition, the *THz wireless*

Optics EXPRESS

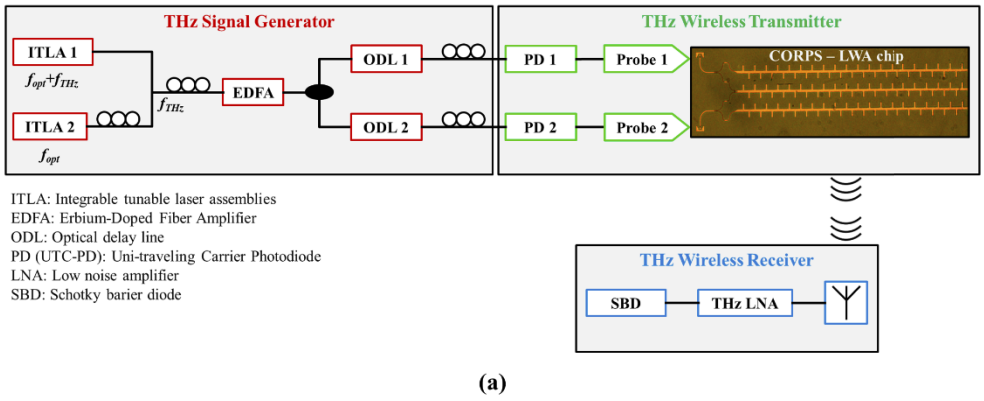


(a)

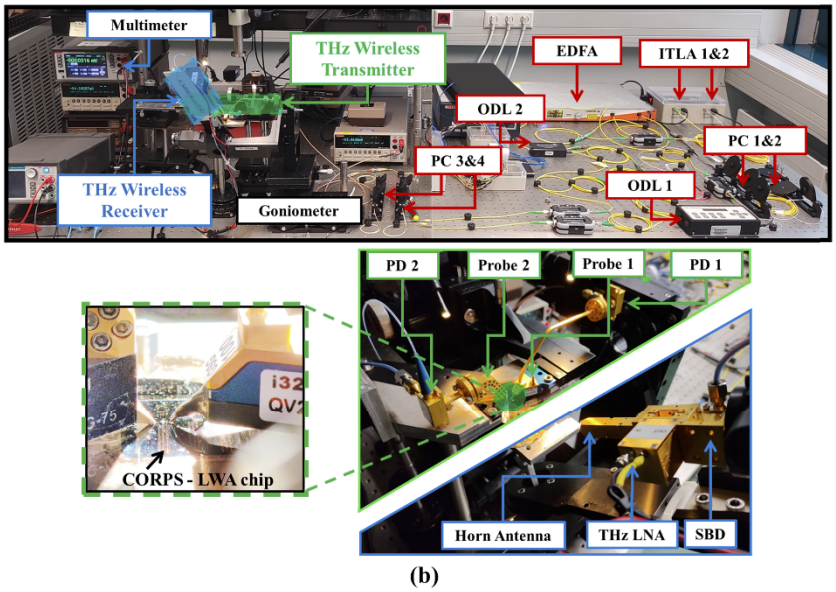


(b)

**Fig. 10.** (a) Schematic diagram of the photonic assisted 2-D beam steering measurement set-up including the THz signal generator (red), THz wireless transmitter (green), and the THz wireless receiver (blue). (b) Measurement set-up for photonic 2D beam steering and zoom-in view of the main components.

*transmitter* is comprised of Ground-Signal-Ground (GSG) WR3.4 probes to feed the THz signals to the respective inputs of the CORPS-BFN. On the *THz wireless receiver* side, a zero-biased Schottky-barrier diode is used as a power detector. The transmitted wireless signal is received by a WR2.8 horn antenna with 26 dBi gain and further amplified using a THz low-noise amplifier (27.5 dB gain). Furthermore, the receiver is installed on a north polar goniometer at the height of ~8 cm above the transmitter, allowing for hemispherical scanning around the transmitter. However, the actual scanning angles are limited mainly by the constructional limitations of the micropositioners and probes (see Fig. 10(b)). Moreover, the poor performance of the on-chip integrated GCPW transition below 0.26 THz and the limited amplification of the LNA below 0.29 THz prevented the full-band frequency characterization. In elevation, the maximum possible scanning angle is from $-15°$ to $+35°$ when $\Delta T = 0$ ps. On the other hand, in azimuth, the maximum scanning angles are $\pm 20°$ for frequencies >0.29 THz.

Optics EXPRESS

To limit the influences of the LWA's first stub, the different path lengths, and any possible fabrication-related impacts of the CORPS-BFN on the desired beam direction of the chip, we moved the receiver to the $E$-plane ($\phi = 0°$, see Fig. 1). Then, the ODL1 is tuned to 2500 fs to steer the main beam in $\phi$-direction to meet the receiver. After that, the delay of ODL1 is increased from 1660 to 3340 fs with a step of 280 fs, i.e., $\Delta T$ will increase from −840 fs to +840 fs.

Figure 11 validates the 2-D beam steering capabilities by plotting the measured beam angle in elevation as a function of the frequency at $\Delta T = 0$ ps; and the beam angle in azimuth as a function of $\Delta T$ at $f = 0.3$ THz. A systematic deviation in the curve slope is observed when comparing the measured beam angles in elevation with the simulated curve. This deviation can be justified by the difference in propagation constants between the fabricated and simulated chips. On the other hand, to seek a fair comparison between simulations and measurements in the azimuth direction, the influence of the first LWA stub is also eliminated in the simulation environment to get $\phi = 0°$ for $\Delta T = 0$. As a result, an excellent overall matching between the measured points and the simulated curve is observed. The measurement system's imperfections can explain the variations between simulations and measurements, i.e., reflections are caused by metallic surfaces – like probes and goniometer arms – which then influence the measurement.

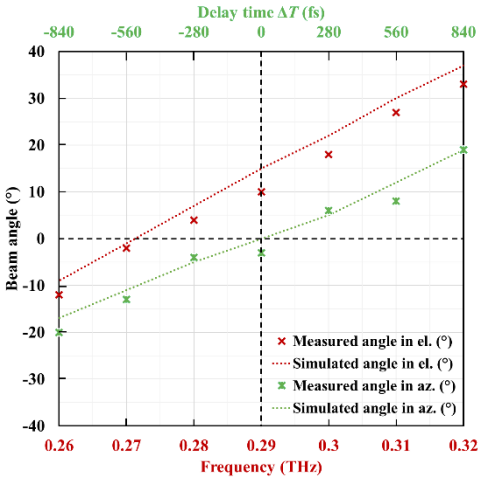


**Fig. 11.** A comparison between the measured and simulated beam angle in elevation direction as a function of frequency (red) and in azimuth direction as a function of $\Delta T$ (green)

The equirectangular projection of the measured normalized beam profile at 0.29 THz, 0.3 THz, and 0.31 THz with three different time delays between the input ports are provided in Fig. 12(a). For $\Delta T = 0$ ps, the beam steers by ∼0.7 °/GHz in $+\theta$ direction when the frequency changes from 0.29 to 0.31 THz. In addition, the beam scans ±10° in $E$-plane with $\Delta T = \pm 0.56$ ps. Figure 12(b) provides a direct comparison for the measured normalized beam profile with the simulated profiles at the same frequencies and time delays.

The experimental characterizations above were carried out using the LWA array with CORPS-BFN fabricated on a quarter InP substrate without dicing. Thus, as previously discussed in [25], a beam profile deformation is expected. In addition, the THz wireless transmitter contains two different probes (GSG FormFactor InfinityProbe and GSG GGB Picroprobe Model 330) and two different NTT-UTC-PDs. Consequently, it was demanding to provide two signals with the same output power from both PDs and keep the relative phase at the input ports of the CORPS-BFN constant.

Optics EXPRESS

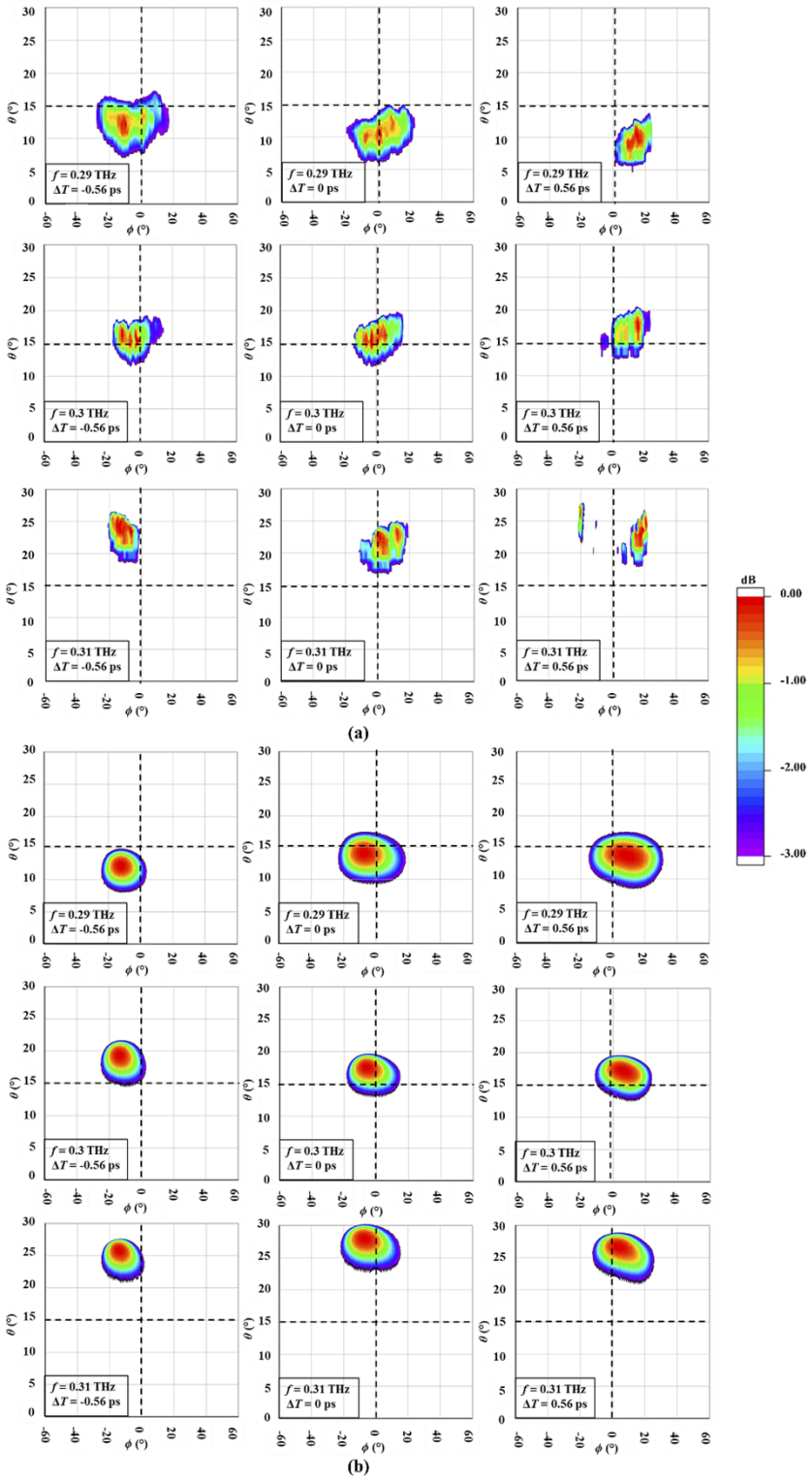


**Fig. 12.** (a) Measured 3-dB beam profile at 0.29 THz, 0.3 THz and 0.31 THz when three different time delays are applied. (b) Simulated 3-dB beam profile at the same frequency and time delays.

Optics EXPRESS

The power deviation can be minimized by characterizing each PD and probe before starting the measurements. Further computational electromagnetics simulations using CST showed that the side effects of a power imbalance on the beam direction are limited and barely affect the angle measurements accuracy. Nonetheless, the realized gain is directly affected by the power available at the CORPS-BFN inputs, which dissipates at the resistors by the unbalanced operation of the WPCD. Consequently, the value of the realized gain will decrease when the signal amplitude/power at the inputs is not the same, resulting in a penalty of 0.4 dBi on the realized gain when the signal's amplitude is halved. On the other hand, degradation of 0.2 dBi was committed when the beam was steered in E-plane for 10° due to applying a delay time of 0.56 ps; this degradation agrees with the efficiency reduction when increasing the scanning angle in CORPS-BFN (as discussed in section 3.2).

Nevertheless, the mentioned impacts provide strong evidence for the necessity of integrating the structure of the CORPS-BFN and LWAs array with PDs on a single chip allowing for high THz input power and better phase control.

## 6. Conclusions

This article presents a novel photonic-assisted 2-D THz beam steering chip based on an array of three LWAs with a monolithically integrated CORPS-BFN with two inputs and three outputs. To our knowledge, this is the first 2-D THz chip-integrated beam steering approach, which requires only two tuning elements: a frequency tunable dual-wavelength laser for elevation control and a TTD for azimuth control.

From full-wave EM simulations for a single LWA, the beam scanning range in elevation, i.e., in $E$-plane, and the realized gain are 92° and 13.7 dBi, respectively. The beam steering in elevation is achieved by tuning the THz frequency between 0.23 and 0.33 THz. To mitigate the OSB of the LWAs, a new antenna design is proposed, including a matching stub in each unit cell of the LWA. As a result, it is shown that the OSB penalty at broadside is mitigated.

In order to steer the beam in azimuth using one tuning element, a new THz $2\times3$ CORPS beamforming network is introduced. The CORPS-BFN provides a linearly progressive phase distribution among its three outputs when tuning the relative phase delay at one of the two input ports. As a result, the total simulated azimuth scanning range reaches 69.18° for a side-lobe suppression of 0 dB. While, for a side-lobe suppression of 10 dB, the entire scanning range in azimuth is still as large as 34°.

The fabricated chip of the LWA array and the CORPS-BFN is characterized using a THz VNA. The isolation and return loss show an excellent agreement with the simulations, fulfilling the 20 dB and 15 dB benchmarks thanks to the developed planar Ti/$TiO_2$ resistors.

The 2-D beam steering capabilities of the system were experimentally investigated using a goniometer. The elevation ($\theta$) and azimuth ($\phi$) scanning angles are validated at different frequencies and delay times. For a time delay $\Delta T = 0$ ps between the two inputs of the CORPS-BFN, the beam scans in elevation between −12° and 33° when sweeping the frequency from 0.26 to 0.32 THz. In azimuth, the beam scans from −19° to +20° when applying a delay difference from −0.84 ps to +0.84 ps. The deviation between the numerically and experimentally determined angles is below 5°.

The presented LWA array and the CORPS-BFN were designed intentionally to allow fabrication on 50 µm thick InP which opens up the possibility of monolithic integration with our 1.55 µm uni-traveling carrier THz photodiodes. This integration would not only result in an ultra-compact photonic integrated THz beam steering transmitter chip (THz Transmitter PIC) but also improve its performance. The beam scanning in elevation will cover the WR3.4 frequency band, which is currently limited by the GCPW-transition >0.26 THz. In addition, the THz input power to the antenna is expected to increase by more than 10 dB due to the monolithic integration. The maximum azimuth scanning range can also be extended by the monolithic integration of

Optics EXPRESS

the structure with photodiodes, as the mechanical constraints of the on-chip GSG probes will be avoided. Such a THz Transmitter PIC may impact various applications such as 6G THz communications, THz imaging and spectroscopy.

**Funding.** Deutsche Forschungsgemeinschaft (Project-ID 287022738– CRC/TRR 196(Project C07)); Bundesministerium für Bildung und Forschung (6GEM, grant No. EFRE-0400215, grant No.16KISK017, grant No.16KISK039, NRW/EFRE Terahertz-Integrationszentrum (THzIZ), Open6GHub); Agencia Estatal de Investigación (/MCIN/AEI/10.13039/501100011033, PID2019-109984RB-C43/AEI/10.13039/501100011033, PID2020-112545RB-C53); Ministerio de Ciencia e Innovación (FPU Program 00013/2018).

**Disclosures.** The authors declare no conflicts of interest.

**Data availability.** Data underlying the results presented in this paper are not publicly available at this time but may be obtained from the authors upon reasonable request.

## References

1. L. Yu, L. Hao, T. Meiqiong, H. Jiaoqi, L. Wei, D. Jinying, C. Xueping, F. Weiling, and Z. Yang, "The medical application of terahertz technology in non-invasive detection of cells and tissues: opportunities and challenges," RSC Adv. **9**(17), 9354–9363 (2019).
2. Y. Zhang, C. Wang, B. Huai, S. Wang, Y. Zhang, D. Wang, L. Rong, and Y. Zheng, "Continuous-Wave THz Imaging for Biomedical Samples," Appl. Sci. **11**(1), 71 (2020).
3. S. E. Hosseininejad, K. Rouhi, M. Neshat, R. Faraji-Dana, A. Cabellos-Aparicio, S. Abadal, and E. Alarcón, "Reprogrammable graphene-based metasurface mirror with adaptive focal point for THz imaging," Sci. Rep. **9**(1), 2868 (2019).
4. P. Liu, Y. Liu, T. Huang, Y. Lu, and X. Wang, "Decentralized automotive radar spectrum allocation to avoid mutual interference using reinforcement learning," IEEE Trans. Aerosp. Electron. Syst. **57**(1), 190–205 (2021).
5. S. Dülme, N. Schrinski, B. Khani, P. Lu, V. Rymanov, A. Stöhr, C. Brenner, and M. R. Hofmann, "Compact Optoelectronic THz Frequency Domain Spectroscopy System for Refractive Index Determination based on Fabry-Perot Effect," in *2018 First International Workshop on Mobile Terahertz Systems (IWMTS)*, (IEEE, 2018), 1–5.
6. L. Liebermeister, S. Nellen, R. B. Kohlhaas, S. Lauck, M. Deumer, S. Breuer, M. Schell, and B. Globisch, "Optoelectronic frequency-modulated continuous-wave terahertz spectroscopy with 4 THz bandwidth," Nat. Commun. **12**(1), 1071 (2021).
7. K. Yamada, Y. Samura, O. V. Minin, A. Kanno, N. Sekine, J. Nakajima, I. V. Minin, and S. Hisatake, "Short-range wireless transmission in the 300 GHz band using low-profile wavelength-scaled dielectric cuboid antennas," Frontiers in Comm. and Net. **2**(2021).
8. J. W. Holloway, G. C. Dogiamis, and R. Han, "Innovations in terahertz interconnects: High-speed data transport over fully electrical terahertz waveguide links," IEEE Microw. Mag. **21**(1), 35–50 (2020).
9. C. Chaccour, M. N. Soorki, W. Saad, M. Bennis, P. Popovski, and M. Debbah, "Seven defining features of terahertz (THz) wireless systems: A fellowship of communication and sensing," IEEE Comm. Surveys & Tutorials (2022).
10. M. Z. Chowdhury, M. Shahjalal, S. Ahmed, and Y. M. Jang, "6G wireless communication systems: Applications, requirements, technologies, challenges, and research directions," IEEE Open J. Commun. Soc. **1**, 957–975 (2020).
11. P. Lu, T. Haddad, J. Tebart, M. Steeg, B. Sievert, J. Lackmann, A. Rennings, and A. Stöhr, "Mobile THz communications using photonic assisted beam steering leaky-wave antennas," Opt. Express **29**(14), 21629–21638 (2021).
12. T. Nagatsuma, G. Ducournau, and C. C. Renaud, "Advances in terahertz communications accelerated by photonics," Nat. Photonics **10**(6), 371–379 (2016).
13. K. Kibaroglu, M. Sayginer, T. Phelps, and G. M. Rebeiz, "A 64-element 28-GHz phased-array transceiver with 52-dBm EIRP and 8–12-Gb/s 5G link at 300 meters without any calibration," IEEE Trans. Microwave Theory Techn. **66**(12), 5796–5811 (2018).
14. T. Ishibashi and H. Ito, "Uni-traveling-carrier photodiodes," J. Appl. Phys. **127**(3), 031101 (2020).
15. P. Latzel, F. Pavanello, M. Billet, S. Bretin, A. Beck, M. Vanwolleghem, C. Coinon, X. Wallart, E. Peytavit, and G. Ducournau, "Generation of mW level in the 300-GHz band using resonant-cavity-enhanced unitraveling carrier photodiodes," IEEE Trans. THz Sci. Technol. **7**(6), 800–807 (2017).
16. J. A. Nanzer, T. P. McKenna, and T. R. Clark, "A W-band photonic array," in *2014 IEEE Antennas and Propagation Society International Symposium (APSURSI)*, (IEEE, 2014), 239–240.
17. S. Makhlouf, M. Steeg, T. Haddad, J. Tebart, S. Dülme, M. Grzeslo, P. Lu, J. L. F. Estévez, S. Malz, and U. R. Pfeiffer, "Novel 3-D Multilayer Terahertz Packaging Technology for Integrating Photodiodes Arrays and Rectangular Waveguide-Power Combiners," IEEE Trans. Microwave Theory Techn. **68**(11), 4611–4619 (2020).
18. C. A. Balanis, "Arrays: Linear planar and circular," in *Antenna theory: analysis and design*, 3rd ed. (John Wiley & Sons, Inc., 2005), pp. 290–398.
19. P. Hall and S. Vetterlein, "Review of radio frequency beamforming techniques for scanned and multiple beam antennas," in *IEE Proceedings H (Microwaves, Antennas and Propagation)*, (IET, 1990), 293–303.
20. Y. J. Guo, M. Ansari, R. W. Ziolkowski, and N. J. Fonseca, "Quasi-Optical Multi-Beam Antenna Technologies for B5G and 6G mmWave and THz Networks: A Review," IEEE Open Journal of Ant. and Prop. (2021).

Optics EXPRESS


21. D. Headland, Y. Monnai, D. Abbott, C. Fumeaux, and W. Withayachumnankul, "Tutorial: Terahertz beamforming, from concepts to realizations," APL Photonics **3**(5), 051101 (2018).
22. Y. Zhou, G. Sakano, Y. Yamanaka, H. Ito, T. Ishibashi, and K. Kato, "600-GHz-wave beam steering by terahertz-wave combiner," in *2018 Optical Fiber Communications Conference and Exposition (OFC)*, (IEEE, 2018), 1–3.
23. K.-i. Maki and C. Otani, "Terahertz beam steering and frequency tuning by using the spatial dispersion of ultrafast laser pulses," Opt. Express **16**(14), 10158–10169 (2008).
24. M. Che, Y. Matsuo, H. Kanaya, H. Ito, T. Ishibashi, and K. Kato, "Optoelectronic THz-wave beam steering by arrayed photomixers with integrated antennas," IEEE Photonics Technol. Lett. **32**(16), 979–982 (2020).
25. P. Lu, T. Haddad, B. Sievert, B. Khani, S. Makhlouf, S. Dülme, J. F. Estévez, A. Rennings, D. Erni, U. Pfeiffer, and A. Stöhr, "InP-based THz beam steering leaky-wave antenna," IEEE Trans. THz Sci. Technol. **11**(2), 218–230 (2021).
26. H. Jalili and O. Momeni, "A 0.34-THz Wideband Wide-Angle 2-D Steering Phased Array in 0.13-$\mu$m SiGe BiCMOS," IEEE J. Solid-State Circuits **54**(9), 2449–2461 (2019).
27. K. Sato and Y. Monnai, "Two-Dimensional Terahertz Beam Steering Based on Trajectory Deflection of Leaky-Mode," IEEE Trans. THz Sci. Technol. **11**(6), 676–683 (2021).
28. D. Betancourt and C. del Río Bocio, "A novel methodology to feed phased array antennas," IEEE Trans. Antennas Propagat. **55**(9), 2489–2494 (2007).
29. G. V. Tsoulos and C. G. Christodoulou, "Arrays and Smart Antennas," in *Modern Antenna Handbook*, C. A. Balanis, ed. (A John Wiley & Sons, inc., publication, 2008), pp. 529–580.
30. W. Stutzman and G. Thiele, "Array antennas," Antenna Theory and Design **3**, 294–295 (2012).
31. D. Pozar, "Considerations for millimeter wave printed antennas," IEEE Trans. Antennas Propagat. **31**(5), 740–747 (1983).
32. S. Paulotto, P. Baccarelli, F. Frezza, and D. R. J. I. T. o. A. Jackson, and Propagation, "A novel technique for open-stopband suppression in 1-D periodic printed leaky-wave antennas," IEEE Trans. Antennas Propag. **57**(7), 1894–1906 (2009).
33. E. J. Wilkinson, "An N-way hybrid power divider," IEEE Trans. Microwave Theory Techn. **8**(1), 116–118 (1960).
34. N. Behdad and M. A. Al-Joumayly, "A generalized synthesis procedure for low-profile, frequency selective surfaces with odd-order bandpass responses," IEEE Trans. Antennas Propagat. **58**(7), 2460–2464 (2010).
35. G. Wang, J. Li, K. Lv, W. Zhang, X. Ding, G. Yang, X. Liu, and X. Jiang, "Surface thermal oxidation on titanium implants to enhance osteogenic activity and in vivo osseointegration," Sci. Rep. **6**(1), 31769 (2016).
36. F. Smits, "Measurement of sheet resistivities with the four-point probe," Bell Syst. Tech. J. **37**(3), 711–718 (1958).
37. M. Kirley and J. H. Booske, "Terahertz conductivity of copper surfaces," IEEE Trans. THz Sci. Technol. **5**(6), 1012–1020 (2015).
38. G. F. Engen and C. A. Hoer, "Thru-reflect-line: An improved technique for calibrating the dual six-port automatic network analyzer," IEEE Trans. Microwave Theory Techn. **27**(12), 987–993 (1979).
39. X. Liu, K. Kolpatzeck, L. Häring, and A. Czylwik, "Experimental Validation of a Phase Control Concept for Photonically Steered Terahertz Phased Array Transmitters at Microwave Frequencies," in *2018 First International Workshop on Mobile Terahertz Systems (IWMTS)*, (IEEE, 2018), 1–5.